Energy & Environmental Science

Synergistic Control of Multilength-Scale Morphology and Vertical Phase Separation for High-Efficiency Organic Solar Cells

Journal:	*Energy & Environmental Science*
Manuscript ID	EE-ART-05-2024-002234.R1
Article Type:	Paper
Date Submitted by the Author:	27-Aug-2024
Complete List of Authors:	Zhou, Xiaoli; Donghua University, College of Materials Science and Engineering Liang, Wenting; Donghua University, College of Materials Science and Engineering Ma, Ruijie; The Hong Kong Polytechnic University, Electrical and Electronic Engineering Zhang, Cuifen; Center for Advanced Low-dimension Materials, Donghua University Peng, Zhengxing; Advanced Light Source Dela Peña, Top Archie; The Hong Kong University of Science and Technology - Guangzhou Campus, Function Hub, Advanced Materials Thrust; The Hong Kong Polytechnic University, Faculty of Science, Applied Physics Wu, Jiaying; The Hong Kong University of Science and Technology - Guangzhou Campus, Advanced Materials Thrust, Function Hub; The Hong Kong University of Science and Technology School of Engineering, Chemical and Biological Engineering Ma, Zaifei; Center for Advanced Low-dimension Materials, Donghua University, Liao, Yaozu; Donghua University, ; Li, Gang; The Hong Kong Polytechnic University, Electronic and Information Engineering Hu, Huawei; Donghua University College of Materials Science and Engineering, ; North Carolina State University, Physics

Broader Context

Organic solar cells (OSCs) have emerged as promising candidates for renewable energy harvesting due to their lightweight, flexibility, and compatibility with large-area, low-cost fabrication processes. However, despite significant advancements in OSC technology, morphology control remains a formidable challenge. The multiscale nature of morphology, ranging from nanometer to micrometer length scales, presents a significant hurdle. Additionally, achieving vertical phase separation, where donor and acceptor materials segregate efficiently to form distinct pathways for charge transport, further complicates the challenge. In this work, by precisely controlling the fluorine content in the side chains, we achieved improved morphology control and vertical phase separation in the active layer of the solar cells. This led to enhanced charge transport properties, reduced trap densities, and decreased non-radiative recombination, ultimately resulting in lower energy losses and improved overall device performance. Our findings suggest that precise control over fluorine content offers new opportunities for tailoring the morphology and performance of OSC devices, paving the way for future advancements in renewable energy harvesting technologies.

Synergistic Control of Multilength-Scale Morphology and Vertical Phase Separation for High-Efficiency Organic Solar Cells

Xiaoli Zhou,‡[a] Wenting Liang,‡[a] Ruijie Ma,[b] Cuifen Zhang,[ac] Zhengxing Peng,[d] Top Archie Dela Peña,[e] Jiaying Wu,[e] Zaifei Ma,[c] Yaozu Liao,[a] Gang Li,[b] Huawei Hu*[a]

[a] State Key Laboratory for Modification of Chemical Fibers and Polymer Materials, College of Materials Science and Engineering, Donghua University, Shanghai 201620, China.

E-mail: huaweihu@dhu.edu.cn

[b] Department of Electrical and Electronic Engineering, Research Institute for Smart Energy (RISE), Guangdong-Hong Kong-Macao (GHM) Joint Laboratory for Photonic-Thermal-Electrical Energy Materials and Devices, The Hong Kong Polytechnic University, Hung Hom, Kowloon, Hong Kong, 999077 P. R. China

[c] Center for Advanced Low-Dimension Materials, Donghua University, Shanghai 201620, China

[d] Advanced Light Source, Lawrence Berkeley National Laboratory, Berkeley, CA 94720, USA

[e] Function Hub, Advanced Materials Thrust, The Hong Kong University of Science and Technology, Nansha, 511400 Guangzhou, P. R. China

‡ X. Z. and W. L. contributed equally to this work

Abstract:

Controlling the morphology of organic solar cells (OSCs) presents a significant challenge due to their complex structure and composition. In particular, attaining synergistic control over both the multi-length-scale morphology and vertical phase separation poses a significant obstacle to the advancement of OSC technology. Here, we designed and synthesized two Y-series acceptors, namely BTP-9F and BTP-17F, with precisely controlled semi-fluorinated side chains attached to the pyrrole rings. The results indicate that BTP-9F-based organic solar cells (OSCs) exhibited more efficient polaron generation dynamics, reduced trap density, and charge recombination due to thieir optimized hierarchical morphology compared to PM6:BTP-17F-based OSCs. Consequently, PM6:BTP-9F-based OSCs achieved a promising power conversion efficiency (PCE) of 17.2%, significantly outperforming PM6:BTP-17F-based devices (14.1%). Furthermore, a remarkable PCE of 19.1%, coupled with an enhanced open-circuit voltage, was achieved in PM6:BTP-eC9:BTP-9F-based ternary systems. This achievement was attributed to the suppression of non-radiative recombination facilitated by synergistically controlled multilength-scale morphology and vertical phase separation. Our work shows that precise manipulation of the semi-fluorinated side-chain of NFAs is a compelling strategy for fine-tuning hierarchical morphology and minimizing energy loss to realize highly efficient OSCs.

Key words: organic solar cells, non-fullerene acceptor, multilength-scale morphology, energy loss, fluorination

1. Introduction

Organic solar cells (OSCs) have emerged as a highly promising frontier in solar technologies, boasting distinctive advantages such as lightweight construction, flexibility, and compatibility with efficient roll-to-roll fabrication processes.[1-5] The field has witnessed intensive research efforts dedicated to material development and device optimization, resulting in remarkable breakthroughs.[6-8] Notably, power conversion efficiencies (PCEs) in non-fullerene acceptors (NFAs) based OSCs have exceeded 19%,[9-13] which has garnered considerable attention from both academic researchers and

the industry. The optimal performance of OSCs is intricately connected to bulk-heterojunction (BHJ) photoactive layer morphology,[14] influenced by factors such as molecular packing, domain purity, and domain size.[15-17]. Besides, the device performance also relies heavily on the vertical phase separation within the active layer. Ideally, donors and acceptors should segregate near the anode and cathode, respectively, enabling efficient hole and electron transport while minimizing charge recombination at the interfaces between the active layer and the electrodes. Although numerous endeavors, including innovative material design and the exploration of cutting-edge fabrication techniques, have been developed to fine-tune the BHJ morphology to achieve higher PCEs,[18-22] effectively manipulating the hierarchical morphology and the vertical phase separation synergistically within the active layer to optimize charge dynamics remains a formidable challenge in the quest for high-efficiency OSCs.[23-25]

The unique characteristics of fluorine, including its small atomic size, strong electronegativity, and unique electronic properties, make it a versatile tool for tailoring the performance of organic semiconductors.[26] When integrated into the backbone or side chains of organic semiconductors, fluorine atoms exert a pronounced influence on the energy levels and molecular packing behavior of the materials.[27] Furthermore, fluorination plays a pivotal role in adjusting the surface energy, a critical factor in achieving the desired BHJ morphology in OSCs fabricated through a solution process. The strategic incorporation of trifluoromethyl groups into the end groups of Y-type NFAs serves as a compelling illustration of the transformative impact of fluorine functionalization on organic semiconductor design, resulting in an ultra-narrow bandgap and 3D interpenetrated molecular stacking.[28] In recent advancements within the Y-series NFAs, a complementary approach involves the incorporation of fluorinated alkyl chains into the pyrrole unit.[29] This strategic implantation is designed to reduce the surface energy of the material, exerting a profound influence on the wetting behavior and thus regulating the vertical phase distribution of the bulk-heterojunction layer. However, an obvious reduction in the open-circuit voltage (V_{OC}) is observed when employing these fluorinated Y-series NFAs in both binary and corresponding ternary systems.[30, 31] This reduction may be attributed to the severe charge recombination

caused by over-fluorination, hindering further advancements in device performance. Furthermore, tuning of molecular packing and phase separation in fluorinated alkyl-containing NFAs presents a significant challenge, since excessive fluorination can result in undesirable morphological characteristics, characterized by large phase separation, thereby compromising the performance of the device.[32] Therefore, it is crucial to precisely control the fluorine functionalization of NFAs as it is a pivotal requirement to strike a delicate balance between surface energy modulation and the preservation of energy loss.

In this work, we systematically designed and synthesized a series of Y-series NFAs with precisely controlled semi-fluorinated alkyl chains on the nitrogen atoms of the pyrrole motif. BTP-9F, featuring an optimal fluorinated side chain, exhibited a larger dipole moment and more rigid molecular packing compared to BTP-17F. Additionally, PM6:BTP-9F-based blend film exhibits an optimal morphology with smaller domain size, and higher domain purity at the smaller length scale. Consequently, PM6:BTP-9F demonstrated faster and more efficient polaron generation dynamics, along with reduced trap density and charge recombination. In contrast to the 14.1% PCE achieved in BTP-17F-based binary devices, the BTP-9F-based binary devices exhibited a promising PCE of 17.2%, showcasing simultaneous improvements in V_{OC}, short-circuit current density (J_{SC}), and fill factor (FF). Furthermore, an outstanding PCE of 19.1% was realized in PM6:BTP-eC9:BTP-9F-based ternary systems, which is attributed to the synergistically controlled multilength-scale morphology and vertical phase separation. The resulting optimal morphology effectively facilitates exciton dissociation and charge collection, while suppressing non-radiative recombination. Our work shows that precise manipulation of side-chain fluorination of NFAs is a compelling strategy to synergistically tune the multilength-scale morphology and vertical phase separation, leading to the realization of highly efficient OSCs.

2. Results and discussion

2.1 Materials synthesis and characterization

The chemical structures of PM6, BTP-9F, and BTP-17F are illustrated in Fig. 1a. The

synthetic pathways for BTP-9F and BTP-17F are elucidated in Scheme S1, with detailed information provided in the Supporting Information. The pivotal DA'D intermediates were synthesized straightforwardly from compound **1**.[33] Subsequently, the DA'D intermediates underwent formylation and Knoevenagel condensation reactions with 2-(5,6-difluoro-3-oxo-2,3-dihydro-1H-inden-1-ylidene)malononitrile (2F-IC) to afford the target materials. Both BTP-9F and BTP-17F exhibit good solubility in commonly used organic solvents. Thermogravimetric analysis (Fig. S1, ESI†) reveals that they decompose at elevated temperatures exceeding 340 ℃, indicating their robust thermal stability. Density functional theory (DFT) calculations at the B3LYP/6-31g(d, p) level were conducted to investigate the influence of the side chain fluorination on the geometries and electrical properties. As shown in Fig. S2 (ESI†), the optimized molecular geometries and spatial distributions of molecular orbitals reveal a noteworthy similarity between the two acceptors, indicating that their fundamental electronic structures share common features. The theoretical lowest unoccupied molecular orbitals (LUMO) and highest occupied molecular orbitals (HOMO) energy levels are estimated to be −3.54/−5.58 and −3.55/−5.60 eV for BTP-9F and BTP-17F, respectively, suggesting a slight downshift in these energy levels after the introduction of additional fluorine atoms in the NFA. Furthermore, the molecular dipole moments and electrostatic potential were simulated (Fig. S3, ESI†). The molecular dipole moments for BTP-9F and BTP-17F were measured to be 1.44 Debye and 1.22 Debye, respectively. The larger dipole moment of BTP-9F suggests a lower driving force for effectively creating charges in donor:acceptor blends, which can be beneficial for achieving higher FF in the devices.[34, 35]

The UV-Vis absorption spectra are performed in both diluted solutions and thin films. Fig. 1b shows that BTP-9F had an absorption peak at 725 nm, which was slightly red-shifted relative to the peak at 721 nm for BTP-17F. The molar extinction coefficients (ε) are found to be 2.21×10^5, and 2.11×10^5 M^{-1} cm^{-1}, for BTP-9F and BTP-17F respectively. In thin film (Fig. 1c), both NFAs had absorption spectra red-shifted relative to those in solution. It is noteworthy that the BTP-9F film had a broader absorption range, which indicates that BTP-9F has stronger intermolecular interactions.

Cyclic voltammetry was carried out to detect the energy levels and the corresponding results are depicted in Fig. 1d and Fig. S4 (ESI†). The LUMO levels were determined to be −3.93 and −3.94 eV for BTP-9F and BTP-17F, respectively. The HOMO levels were determined to be −5.68 eV and −5.71 eV for BTP-9F and BTP-17F, respectively (Table S1, ESI†). The cyclic voltammetry measurement results are consistent with the theoretical calculations.

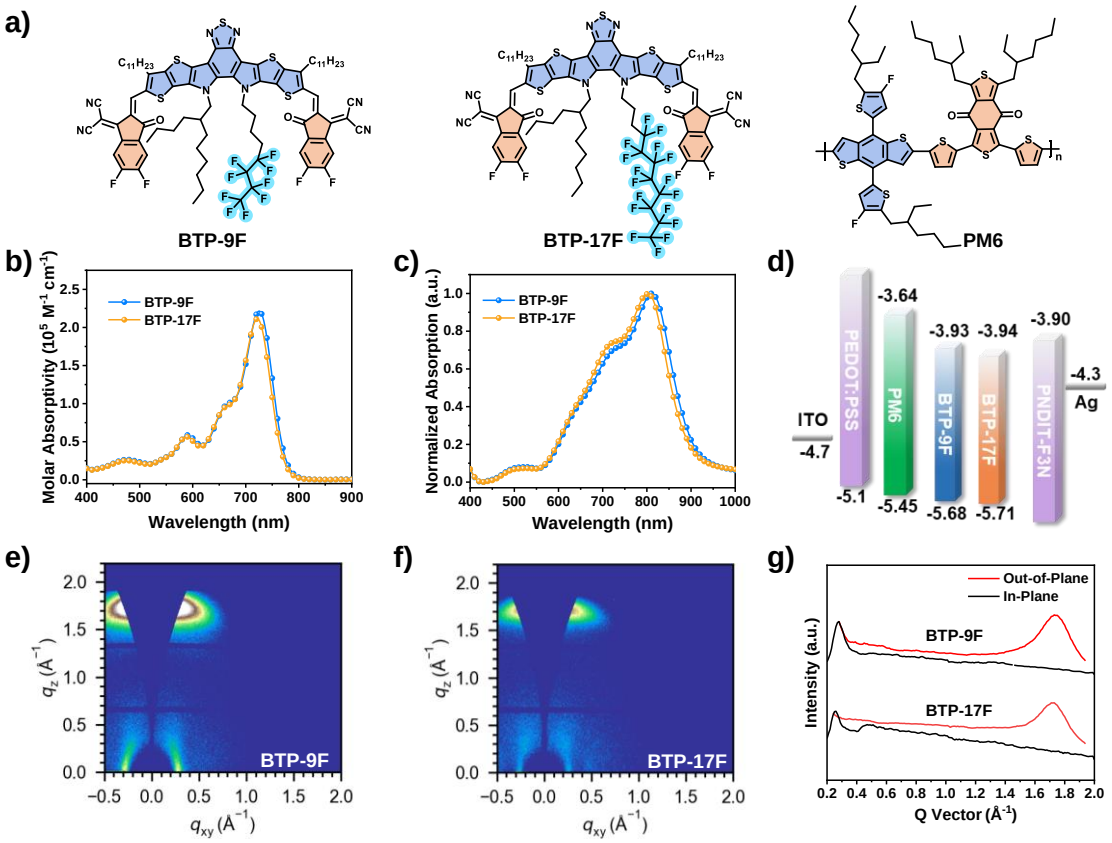

Fig. 1 (a) Chemical structures of BTP-9F, BTP-17F, and PM6. (b) Absorption spectra in chloroform solution. (c) Normalized absorption spectra of pure films; (d) Energy level diagram of the materials used in device fabrication. 2D GIWAXS patterns of the neat (e) BTP-9F and (f) BTP-17F films. (g) 1D profiles along the IP and OOP directions.

The influence of the side chain fluorination on the molecular packing behavior of the acceptors was investigated using grazing-incidence wide-angle X-ray scattering (GIWAXS). The two-dimensional (2D) patterns, as depicted in Fig. 1e and 1f, reveal distinct π–π stacking (010) diffraction signals in the out-of-plane (OOP) direction for both BTP-9F and BTP-17F films, indicative of a preferential face-on orientation

concerning the substrate. Noteworthy differences emerge in the intensity of the diffraction peak, with BTP-9F exhibiting a more pronounced signal compared to BTP-17F, suggesting a more orderly molecular packing structure in the BTP-9F film. Further insight into the molecular packing is gleaned from the one-dimensional (1D) profiles extracted along the OOP direction (Fig.1g). The calculated π–π stacking distances for BTP-9F and BTP-17F films are 3.59 and 3.61 Å in Table S2 (ESI†), respectively. Additionally, the crystal coherence lengths (CCL) are found to be 36.3 and 33.9 Å for BTP-9F and BTP-17F, respectively. The observed differences suggest a higher degree of structural order and tighter packing in BTP-9F, indicative of a more favorable arrangement for charge transport.[36]

2.2 Photovoltaic performances and charge dynamics

The photovoltaic properties were investigated by a conventional device structure of ITO/2PACz/active layer/PNDIT-F_3N/Ag (Fig. 2a), where PM6 was selected as the electron donor material owing to its complementary absorption and matched energy levels. Detailed device fabrication and characterizations are provided in the Supporting Information. Fig. 2b provides the *J*-*V* curves of the optimal OSCs under AM 1.5G solar simulator, and the relevant photovoltaic parameters are summarized in Table 1. The PM6:BTP-17F device obtained a PCE of 14.1%, with a *Voc* of 0.832 V, a J_{SC} of 25.2 mA cm^{-2}, and a FF of 66.8%. In the OSCs utilizing BTP-9F as the acceptor, V_{OC} unexpectedly increases to 0.848 V, which is 16 meV higher than that of the BTP-17F-based device. The J_{SC} and FF are recorded as 27.0 mA cm^{-2} and 75.1%, respectively. Consequently, a promising PCE of 17.2% is achieved for the PM6:BTP-9F-based OSC. In pursuit of further enhancing the photovoltaic properties, we introduced BTP-eC9 (chemical structure and absorption propriety are shown in Fig. S5, ESI†), a third component with molecular structures closely resembling those of BTP-9F. The strategic introduction of BTP-eC9 aims to leverage the similarities in molecular structures between BTP-9F and BTP-eC9, potentially facilitating the formation of alloy-like composites. This, in turn, has the potential to finely tune the active layer morphology, ultimately leading to improved device performance. The minimal charge transfer

between the acceptors, as indicated by the *J*–*V* measurements of the device consisting solely of the acceptors (Fig. S6, ESI†), further supports this hypothesis. The OSCs based on the binary blend of PM6:BTP-eC9 demonstrated a commendable PCE of 18.0%, accompanied by a V_{OC} of 0.846 V, a J_{SC} of 27.6 mA cm^{-2}, and an FF of 77.2%, which is comparable with previously reported results.[37] The ternary device, with 20% BTP-9F (Table S3, ESI†), exhibited the best PCE of 19.1% with a V_{OC} of 0.850 V, a J_{SC} of 28.0 mA cm^{-2}, and a FF of 79.9%. The improved device performance can be attributed to the synergistic effects arising from the combination of BTP-9F and BTP-eC9. The alloy-like composites formed through their similar molecular configurations contribute to a finely tuned active layer morphology, optimizing charge transport and minimizing losses. To corroborate the reliability of the *J*–*V* results, external quantum efficiency (EQE) spectra measurements were conducted for the optimized devices. All devices under investigation demonstrated broad photo-response spanning the range of 400–900 nm, as illustrated in Fig. 2c. The integrated current density values obtained from the EQE spectra, as detailed in Table 1, closely align with the J_{SC} results derived from the *J*–*V* curves (within 5% mismatch).

To evaluate performance degradation, we assessed the stability of the OSCs by exposing encapsulated solar cells to ambient air under 100 mW cm^{-2} white LED light at the maximum power point (MPP). As illustrated in Fig. S7 (ESI†), all binary OSCs exhibited comparable stability, with the PCE maintaining over 70% of its initial value after 300 hours of continuous operation. In contrast, the ternary system devices exhibited notably enhanced photostability, retaining over 80% of their initial PCE over the same period. The improved stability in the ternary devices might be due to denser molecular packing within the active layer, which reduces water and oxygen penetration, thus minimizing morphological changes and enhancing photostability.

Table 1. The optimal photovoltaic parameters of BTP-9F, and BTP-17F-based OCSs.

Active layer	V_{OC} (V) [a)]	J_{SC} (mA cm^{-2})	J_{sat} (mA cm^{-2})	FF (%)	PCE (%)
PM6: BTP-9F	0.848 [0.848±0.003]	27.0 [26.5±0.3]	26.0	75.1 [74.7±0.3]	17.2 [16.8±0.4]
PM6: BTP-17F	0.832 [0.832±0.002]	25.2 [24.8±0.4]	24.8	66.8 [66.3±0.5]	14.1 [13.8±0.3]
PM6: BTP-eC9	0.846 [0.846±0.002]	27.6 [27.3±0.4]	26.8	77.2 [76.8±0.4]	18.0 [17.7±0.3]
PM6: BTP-eC9: BTP-9F	0.850 [0.850±0.002]	28.0 [27.5±0.5]	27.3	79.9 [79.5±0.4]	19.1 [18.7±0.4]

[a)] average values and standard deviations were obtained from over 10 individual devices.

Photovoltaic performances in different devices are investigated by charge recombination and exciton dissociation.[38, 39] The dependence of J_{SC} on the light intensity (P_{light}) was examined to explore the biomolecular recombination behavior using the equation $J_{SC} \propto P^{\alpha}$, where the recombination is negligible if the exponential factor α is 1. Fig. 2d reveals that effectively suppressed bimolecular recombination can be realized in all optimized devices. According to the correlations between V_{OC} and P_{light} of devices as shown in Fig. 2e, $V_{OC} \propto nkT/q \ln(P_{\text{light}})$, the slope factors ($n$) of PM6:BTP-9F, PM6:BTP-17F, PM6:BTP-eC9, and the ternary devices are 1.09, 1.40, 1.04, and 1.01, respectively, suggesting that the use of BTP-9F could potentially reduce trap-assisted recombination in both binary and ternary systems. It is noted that the BTP-17F-based binary blend exhibited significant charge recombination, which may be attributed to improper phase separation within the active layer caused by excessive fluorination.[40, 41] To assess the trap density within the blend films, we conducted a quantitative measurement of the trap density of states (tDOS) using thermal admittance spectroscopy (TAS).[42, 43] Fig. 2f shows that the PM6:BTP-9F-based device exhibited a

trap density of (3.1–7.5)×10^{15} cm^{-3} eV^{-1} at the energy depth of 0.15–0.30 eV, which is much lower than that of (0.4–1.5)×10^{16} cm^{-3} eV^{-1} for PM6:BTP-17F-based OSCs. The PM6:BTP-eC9:BTP-9F-based ternary devices has the lowest trap density of (2.1–8.1)×10^{15} cm^{-3} eV^{-1}. These findings highlight the effectiveness of tailoring the side-chain fluorination of NFAs in suppressing trap density, contributing to increased mobility and inhibited charge-carrier recombination in the device.[44]

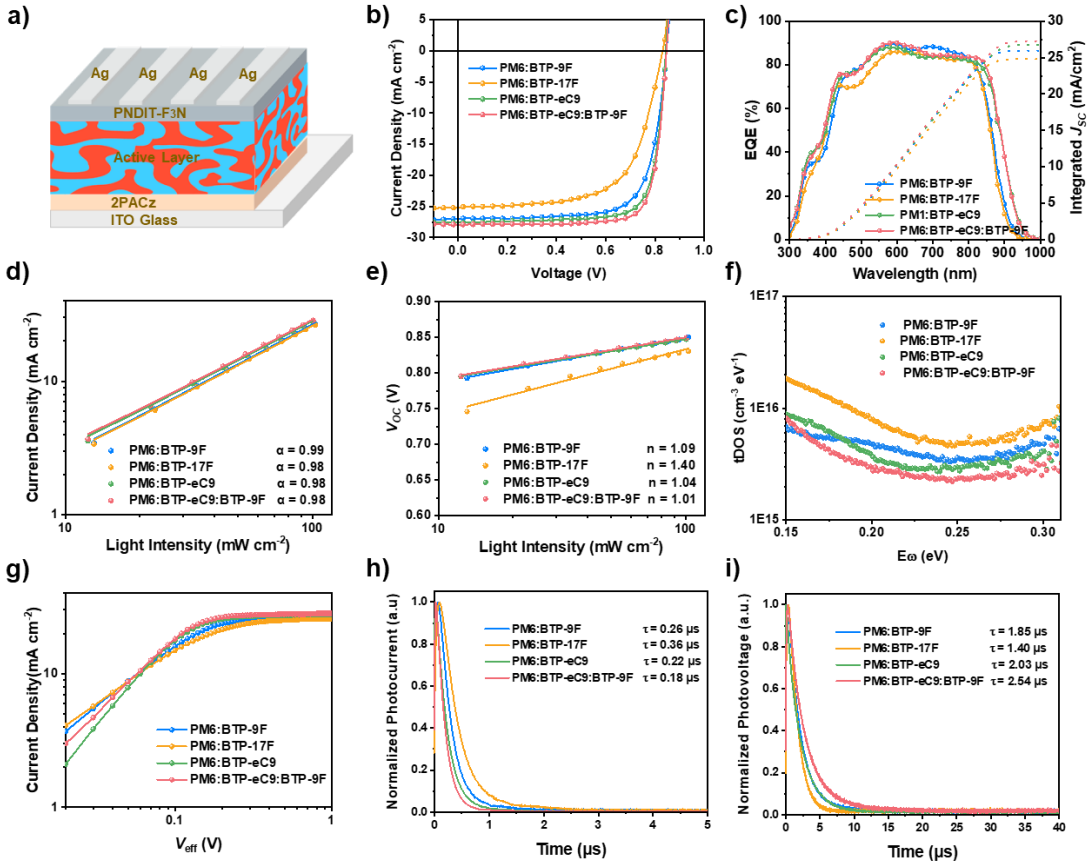

Fig. 2 (a) Schematic diagram of device structure in this work. (b) Current density-voltage (*J*-*V*) curves; (c) EQE spectra and integrated J_{SC} of corresponding devices; (d) J_{SC} versus light intensity of these devices; (e) V_{OC} versus light intensity of these devices; (f) Trap density of states spectra of these devices; (g) J_{ph}–V_{eff} relationships; (h) Transient photocurrent decay curves. (i) Transient photovoltage decay curves.

Furthermore, the relationship between the photocurrent density (J_{ph}) and effective voltage (V_{eff}) is investigated.[45] As seen from Fig. 2g and Table S4 (ESI†), J_{ph} increases with V_{eff} in the low-effectiveness region and reaches a saturated photocurrent density

(J_{sat}) at a high V_{eff} of 2 V for all these devices, indicating that excitons can be effectively dissociated into free charge carriers and then collected by the electrodes. The exciton dissociation probability (P_{diss}) and charge collection efficiency (P_{coll}) were calculated using the formula J/J_{sat}, where J is the photoinduced current under the condition of a short circuit for P_{diss} and the maximum output power for P_{coll}. The P_{diss} values for PM6:BTP-9F, PM6:BTP-17F, PM6:BTP-eC9, and the ternary devices are found to be 98.7%, 97.9%, 98.8%, and 99.4%, respectively, suggesting that better exciton dissociation occurs in the BTP-9F-based OSCs. In addition, the P_{coll} values are found to be 88.3% for PM6:BTP-9F, 81.3% for PM6:BTP-17F, 90.3% for PM6:BTP-eC9 and 91.2% for the ternary devices. Higher P_{diss} and P_{coll} values indicate more efficient photoinduced exciton dissociation and charge collection in the optimal PM6:BTP-eC9:BTP-9F ternary blend, thus contributing to a higher J_{SC} and FF.

Next, the transient photocurrent (TPC) and the transient photovoltage (TPV) experiment for these acceptors are performed to investigate the charge extraction and recombination process.[46, 47] As shown in Fig. 2h, the charge sweep-out time of PM6:BTP-9F, PM6:BTP-17F, PM6:BTP-eC9, and PM6:BTP-eC9:BTP-9F are found to be 0.26, 0.36, 0.22, and 0.18 μs, respectively. In addition, Fig. 2i illustrates that the charge carrier lifetime for PM6:BTP-9F, PM6:BTP-17F, PM6:BTP-eC9, and PM6:BTP-eC9:BTP-9F-based devices are extracted to be 1.85, 1.40, 2.03, and 2.54 μs, respectively. The observed faster charge sweep-out and longer charge carrier lifetime for the PM6:BTP-9F system in comparison to PM6:BTP-17F indicate a larger charge extraction capability for the materials with optimal side chain fluorination.[48] The ternary OSC comprising PM6:BTP-eC9:BTP-9F exhibits superior charge extraction efficiency and longer charge carrier lifetime, which supports the notion that the addition of BTP-9F contributes synergistically to optimizing the charge dynamics within the ternary device.[20]

The dynamics of charge carriers were then investigated using femtosecond transient absorption spectroscopy (fs-TAS).[49, 50] Selective excitation of the acceptor molecules was achieved with an 800 nm laser pump. The acceptor singlet excitons will display ground state bleaching (GSB) at a wavelength range corresponding to the acceptor

ground state absorption. Fig. 3 illustrates positive photo-bleach (PB) signals at ~620–670 nm in these blend films, indicative of hole transfer from the acceptor to the donor within the donor ground state absorption range. Based on Fig. 3a and 3b, both PM6:BTP-9F and PM6:BTP-17F exhibit polaron features at 0.1 ps after excitation, implying the existence of ultrafast free charge generation component.[51] However, such ultrafast polarons PB intensity is more substantial for the case of PM6:BTP-9F. Likewise, relative to the corresponding singlet excitons GSB intensity, the maximum polarons PB intensity for PM6:BTP-9F is higher than PM6:BTP-17F (Fig. S8, ESI†). Considering the higher EQE and J_{SC} for PM6:BTP-9F than that of PM6:BTP-17F, it is then suggestive that PM6:BTP-17F suffers from larger geminate losses from the recombination of singlet excitons which explains its lower P_{diss}. Based on the polarons kinetics (Fig. 3c), the polarons generation dynamics for PM6:BTP-9F is faster than PM6:BTP-17F. This is also consistent with the above discussions wherein the free charge generation for PM6:BTP-9F is more efficient. In addition, the polarons recombination dynamics at the sub-ns range appear comparable, suggesting the comparable bimolecular recombination strength between the two samples. Hence, the difference in their FFs can be assigned to monomolecular recombination such as trap-induced recombination dominating at longer time scales, in line with the reduced trap density for PM6:BTP-9F-based devices as discussed above. The less efficient free-charge transport and higher geminate losses in PM6:BTP-17F can also partially explain the V_{OC} difference owing to the recombination component of energy losses.[52] Fig. 3d and 3e show that the polaron generation behavior is enhanced in the ternary system compared to the binary PM6:BTP-eC9. Figure 3f demonstrated that the ternary system exhibits slower polaron recombination dynamics, which explains the enhanced FF for the PM6:BTP-eC9:BTP-9F ternary OSC device.

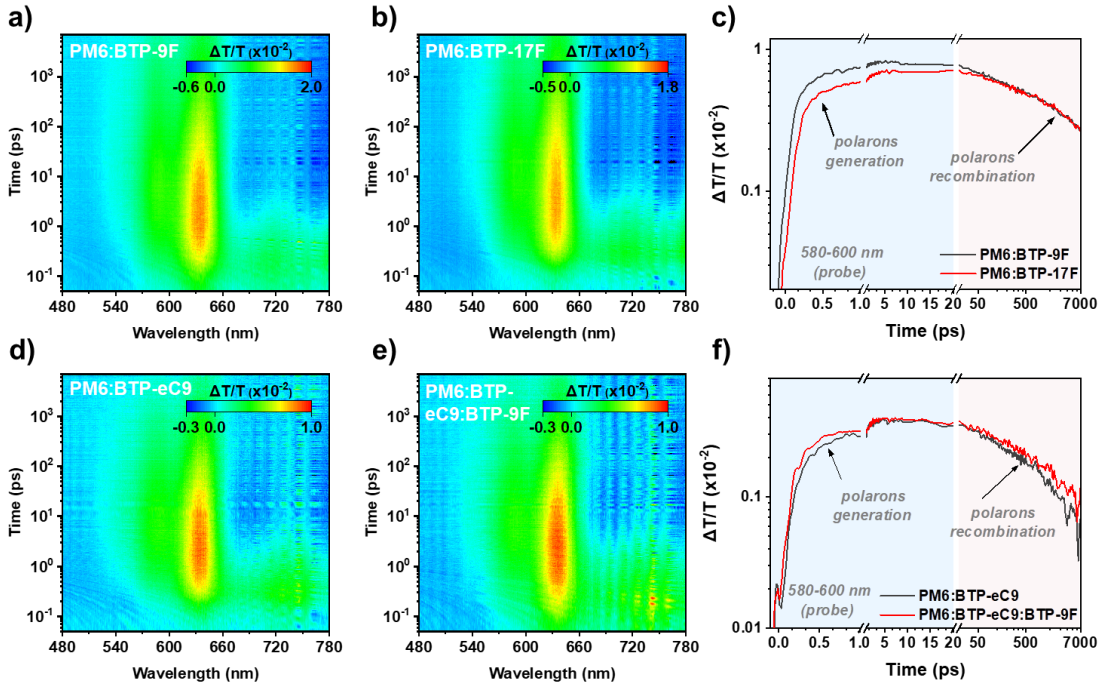

Fig. 3 2D Femtosecond transient absorption spectroscopy of (a) PM6:BTP-9F, (b) PM6:BTP-17F, (d) PM6:BTP-eC9, and (e) ternary blend films pumped at 800 nm. The polarons generation and recombination dynamics for (c) PM6:BTP-9F and PM6:BTP-17F-based blends, (f) PM6:BTP-eC9 and ternary blend films.

To explore the charge-transport properties of the blend films, the space-charge-limited current method was utilized to study the hole and electron mobilities in the binary and ternary systems.[53] As shown in Fig. S9 and Table S5 (ESI†), the average hole/electron mobility (μ_h/μ_e) of PM6:BTP-9F, PM6:BTP-17F, PM6:BTP-eC9, and PM6:BTP-eC9:BTP-9F-based devices are estimated to be $4.0\times10^{-4}/3.5\times10^{-4}$, $2.9\times10^{-4}/2.2\times10^{-4}$, $4.9\times10^{-4}/4.4\times10^{-4}$, and $7.0\times10^{-4}/6.6\times10^{-4}$ $cm^2\ V^{-1}\ s^{-1}$, respectively corresponding to μ_h/μ_e of 1.14, 1.32, 1.11 and 1.06. The solar cell incorporating BTP-9F shows higher and more balanced charge carrier mobilities when compared to those based on the over-fluorinated electron acceptor BTP-17F. Notably, the ternary device stands out with the highest and most balanced charge mobilities. The results emphasize the importance of optimal side-chain fluorination in tailoring the charge transport properties of NFA-based devices, contributing to a more favorable charge transport within the device.

2.3 Blend morphology characterization

The atomic force microscopy (AFM) images as shown in Fig. S10 (ESI†) provide a detailed examination of the surface morphology of the blend films. Height images reveal relatively smooth surfaces for all of these films, with root-mean-square roughness (R_q) values of 1.21 nm for PM6:BTP-9F, 0.97 nm for PM6:BTP-17F, 1.04 nm for PM6:BTP-eC9, and 1.10 nm for the ternary films, respectively. The phase images show a fiber-like network for all these films. Notably, the films based on PM6:BTP-eC9:BTP-9F exhibit thicker fibers compared to the other films, which could potentially enhance exciton dissociation efficiency and facilitate efficient charge transfer pathways.[54, 55] The homogeneous film-morphology was further confirmed by transmission electron microscopy images (Fig. S11, ESI†). GIWAXS experiment (Fig. 4a) shows that all these blend films also exhibit preferential face-on orientation. Specifically, PM6:BTP-9F and PM6:BTP-17F exhibit well-defined π-π stacking peaks at q_{xy} = ~1.70 Å^{-1}, and lamellar peaks at q_{xy} = ~0.28 Å^{-1}, respectively. Moreover, multi-peak fitting (Fig. S12, ESI†) and Table S6 (ESI†) reveal that PM6 has the CCL_{010} of 31.3 and 28.1 Å, and the two acceptors have the CCL_{010} of 35.2 and 33.1 Å for PM6:BTP-9F and PM6:BTP-17F-based films, respectively. The more compact and longer-range ordered π-π packing in the BTP-9F-based binary films is indicative of a favorable morphology for charge transport. With the incorporation of BTP-9F into the PM6:BTP-eC9 blends, the ternary blend films maintained compact π–π stacking. Moreover, CCL_{010} for PM6/NFAs are 18.8/31.3 Å and 28.6/37.5 Å for PM6:BTP-eC9 and PM6:BTP-eC9:BTP-9F-based ternary films, indicating an improvement in molecular ordering with the addition of BTP-9F. This enhanced molecular ordering of BTP-eC9 in the presence of BTP-9F is further confirmed by the GIWAXS patterns of the neat BTP-eC9 and BTP-eC9:BTP-9F based films (Fig. S13, Table S2, ESI†). The ternary blend film exhibits the largest π-π stacking CCLs among the four blends, accounting for its higher J_{SC} and FF mentioned above. Furthermore, resonant soft X-ray scattering (RSoXS) indicates that all the blend films exhibit multilength scale morphology (Fig. 4b), as evidenced by the presence of low-q and high-q peaks. More importantly, the BTP-9F-based binary and ternary films obtained relatively smaller domain sizes and relatively higher domain purity at the smaller length scale (Table S7,

ESI†), which is close to the exciton diffusion length. This facilitates exciton diffusion and suppresses charge recombination, ultimately leading to enhanced device performance.

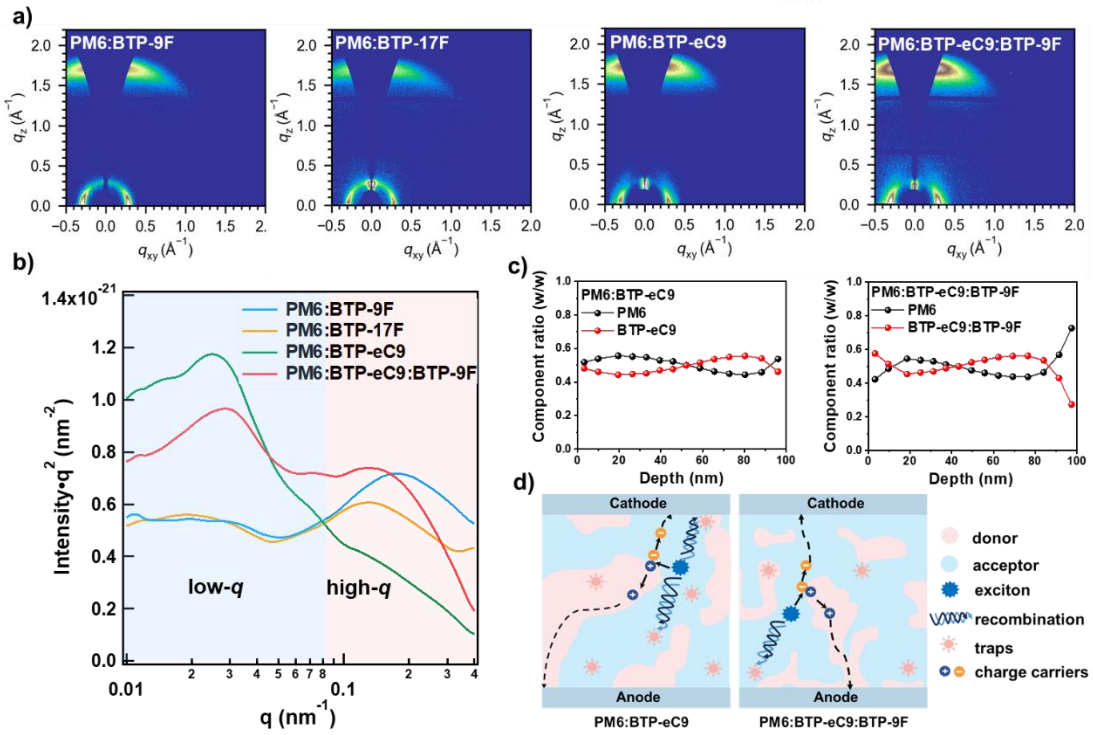

Fig. 4 (a) 2D GIWAXS patterns. (b) RSoXS scattering profiles. (c) Derived weight-ratio vertical distribution within the blend films. (d) Schematic diagram of blend morphology evolution and the related behaviors of exciton and charge carriers.

Film-depth-dependent light absorption spectroscopy (FLAS) was then performed to investigate the phase distribution in the vertical direction.[17, 56] The results are presented in Fig. S14 (ESI†) and the composition weight ratio within PM6:BTP-eC9, PM6:BTP-eC9:BTP-9F-based blends is provided in Fig. 4c. In the case of PM6:BTP-9F and PM6:BTP-17F blend films, it is observed that the NFA is concentrated on the surface layer, while PM6 is enriched in the bottom part of the active layer. While for PM6:BTP-9F-based blend film, it exhibits relatively uniform distribution of donor and NFA across the active layer. In contrast, upon the incorporation of BTP-9F into the PM6:BTP-eC9 blends, the NFA tends to migrate towards the top surface, creating a favorable vertical phase separation that enhances charge transport and collection,[17] as supported by the charge-generation maps shown in Fig. S15 (ESI†). The favorable vertical phase

separation should be attributed to its lower surface energy and its higher miscibility with BTP-eC9. To further confirm this phenomenon, the surface free energy (γ) of these materials is studied by the contact angle measurement.[57] As shown in Fig. S16 and Table S8 (ESI†), there is an increase in the contact angle from BTP-eC9 to BTP-9F and to BTP-17F. The γ values were 25.98, 32.44, 18.25, and 15.58 mJ m^{-2} for PM6, BTP-eC9, BTP-9F, and BTP-17F, respectively. In addition, the introduction of BTP-9F into the PM6:BTP-eC9 host blend resulted in a ternary blend film having a reduced γ value of 25.60 mJ m^{-2} compared to that of 27.85 mJ m^{-2} for PM6:BTP-eC9 based binary system. These results suggest that the NFA are enriched on top of the surface, which is consistent with the FLAS results. Overall, the GIWAXS, RSoXS, and FLAS measurements consistently indicate that manipulation of the semi-fluorinated side chain of NFAs results in an optimal morphology characterized by more ordered molecular packing, optimal domain size, higher domain purity at smaller length scales, and improved vertical phase distribution (Fig. 4d). These improvements contribute to a reduced trap density, increased exciton dissociation, and enhanced charge transport, ultimately leading to improved device performance for the BTP-F9-based binary and ternary OSCs.[58, 59]

2.4 Energy loss analysis and application scope

Addressing the challenge of minimizing energy loss (E_{loss}) is crucial for fluorinated NFAs. To further investigate the underlying reasons for E_{loss} in these side chain fluorinated materials, the detailed E_{loss} was assessed using sensitive EQE (sEQE) and electroluminescence (EL) measurements.[60] According to Fig. S17 (ESI†) and Fig. 5a-d, the band gaps and charge-transfer state energy (E_{CT}) are determined to be 1.457/1.346, 1.466/1.352, 1.428/1.327, and 1.428/1.327 eV for PM6:BTP-9F, PM6:BTP-17F, PM6:BTP-eC9, PM6:BTP-eC9:BTP-9F-based devices, respectively. PM6:BTP-9F exhibits reduced energetic differences (ΔE_{CT}) of 0.111 eV compared with 0.114 eV for PM6:BTP-17F-based devices. Fig. 5e shows that the PM6:BTP-9F and PM6:BTP-eC9-based binary devices exhibit low E_{loss} of 0.609 and 0.582 eV, respectively, which are much lower than that of the PM6:BTP-17F-based blend (0.634 eV). The PM6:BTP-

eC9:BTP-9F-based ternary blend exhibits the minimum E_{loss} of 0.578 eV. The energy loss for the device can be divided into three parts (ΔE_1, ΔE_2, and ΔE_3) according to the Shockley–Queisser (SQ) theory, where ΔE_1 and ΔE_2 are related to radiative recombination above and below the bandgap, respectively.[61] While ΔE_3 represents the nonradiative energy loss, which impacts the overall E_{loss} of an OSC significantly. Table S9 (ESI†) shows that the ΔE_1 values of the four OSCs are quite similar. The ΔE_2 value of PM6:BTP-9F (0.079 eV) is slightly lower than that of PM6:BTP-17F-based devices (0.083 eV), indicating the energy offset could be finely tuned by manipulation of side-chain fluorination. The non-radiative recombination loss of the devices was obtained by the external quantum efficiency of EL (EQE_{EL}, Fig. 5f),[62, 63] from which the ΔE_3 values of 0.264, 0.285, 0.246, and 0.245 eV were achieved for PM6:BTP-9F, PM6:BTP-17F, PM6:BTP-eC9, PM6:BTP-eC9:BTP-9F-based OSCs, respectively. This result demonstrates that the optimal side chain fluorination can effectively suppress the non-radiative recombination, contributing to a lower E_{loss}.

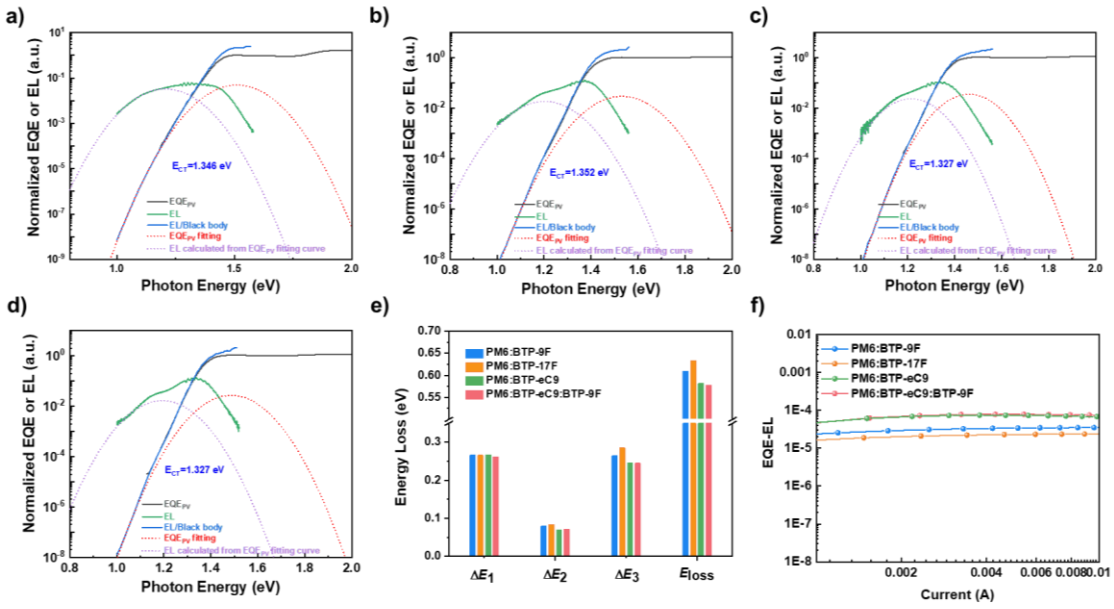

Fig. 5 Semi-logarithmic plots of the EL, sensitive and calculated EL and EQE as a function of energy for (a) PM6:BTP-9F, (b) PM6:BTP-17F, (c) PM6:BTP-eC9, and (d) PM6:BTP-eC9:BTP-9F. (e) Detailed energy loss for these devices. (f) EQE_{EL} dependence on the current of the corresponding materials-based solar cells.

Motivated by the remarkable success of the strategy in optimizing multilength-scale

morphology and vertical phase separation, BTP-9F was integrated into the PM6:Y6 system, resulting in a significant enhancement of the FF for the corresponding ternary device. This modification also induced a slightly increase in the V_{OC}, culminating in a PCE of 18.1% (Fig. S18a and Table S10, ESI†). Additionally, BTP-9F was further incorporated into the PM6:L8-BO-based system. The resulting ternary device exhibited an elevated PCE of 18.9%, accompanied by a markedly improved FF compared to the binary counterpart (Fig. S18b and Table S10, ESI†). These findings demonstrate the efficacy of BTP-9F in optimizing the photovoltaic performance of diverse OSC, underscoring its potential as a versatile ternary component for advancing OSC efficiency.

3. Conclusion

In conclusion, two Y-series NFAs, BTP-9F, and BTP-17F, with precisely controlled semi-fluorinated side chains attached to the pyrrole rings were designed and synthesized. BTP-9F exhibits larger dipole moments and enhanced molecular packing than that of BTP-17F. Moreover, faster efficient polaron generation dynamics, and reduced trap density charge recombination were observed in the blend film, leading to efficient charge transport and reduced energy loss. As a result, a promising efficiency of 17.2% with a high V_{OC} of 0.848 V was achieved in PM6:BTP-9F-based devices, while the PM6:BTP-17F-based OSCs only get a PCE of 14.1% with a lower V_{OC} of 0.832 V. Additionally, PM6:BTP-eC9:BTP-9F-based ternary OSC achieved an outstanding PCE of 19.1%, benefiting from the synergistically manipulated multilength-scale morphology and vertical phase separation. The success of precise manipulation of side-chain fluorination of NFAs is expected to inspire the community to develop new NFAs to finely tune the electronic and hierarchical morphology in the active layer, which is expected to pave the way for further advancements in device performance in the near future.

Author contributions

X. Z. and W. L. contributed equally to this work. X. Z. carried out the materials

synthesis and characterization. W. L. and R. M. carried out the device fabrication and measurements. C.Z. and Z. M. performed the energy loss measurements. Z.P. performed the RSoXS measurements. X. Z. and H.H. prepared the manuscript. Z. M., Y. L., G. L. and H.H. directed and supervised the project. All the authors discussed and commented on the manuscript.

Acknowledgements

The work described in this paper was supported by the National Natural Science Foundation of China (No. 22475037 and 52103202), the Fundamental Research Funds for the Central Universities (2232023A-01), and the Key Laboratory of Fluorine and Silicon for Energy Materials and Chemistry of Ministry of Education, Jiangxi Normal University (no. KFSEMC-202202). We also would like to express our gratitude to beamline BL16B1 and BL02U2 at Shanghai Synchrotron Radiation Facility (SSRF) for their support during the GIWAXS experiment. RSoXS measurement was conducted at ALS BL 11.0.1.2, supported by the Office of Science, Office of Basic Energy Sciences, of the U.S. Department of Energy under Contract No. DE-AC02-05CH11231.

Conflict of Interest

The authors declare no conflict of interest.

Data Availability Statement

The data that support the findings of this study are available from the corresponding author upon reasonable request.

References:

1. L. Meng, Y. Zhang, X. Wan, C. Li, X. Zhang, Y. Wang, X. Ke, Z. Xiao, L. Ding, R. Xia, H.-L. Yip, Y. Cao and Y. Chen, *Science*, 2018, **361**, 1094-1098.
2. R. Søndergaard, M. Hösel, D. Angmo, T. T. Larsen-Olsen and F. C. Krebs, *Mater. Today*, 2012, **15**, 36-49.
3. Y. Liu, J. Zhao, Z. Li, C. Mu, W. Ma, H. Hu, K. Jiang, H. Lin, H. Ade and H. Yan, *Nat. Commun.*, 2014, **5**, 5293.
4. G. Zhang, F. R. Lin, F. Qi, T. Heumuller, A. Distler, H. J. Egelhaaf, N. Li, P. C. Y. Chow, C. J. Brabec, A. K. Jen and H. L. Yip, *Chem Rev*, 2022, **122**, 14180-14274.
5. H. Chen, R. Zhang, X. Chen, G. Zeng, L. Kobera, S. Abbrent, B. Zhang, W. Chen, G. Xu, J. Oh, S.-H. Kang, S. Chen, C. Yang, J. Brus, J. Hou, F. Gao, Y.

Li and Y. Li, *Nat. Energy*, 2021, **6**, 1045-1053.
6. Q. Wei, J. Yuan, Y. Yi, C. Zhang and Y. Zou, *Nat. Sci. Rev.*, 2021, **8**, nwab121.
7. C. Yan, S. Barlow, Z. Wang, H. Yan, A. K. Y. Jen, S. R. Marder and X. Zhan, *Nat. Rev. Mater.*, 2018, **3**, 18003.
8. G. Zhang, J. Zhao, P. C. Y. Chow, K. Jiang, J. Zhang, Z. Zhu, J. Zhang, F. Huang and H. Yan, *Chem. Rev.*, 2018, **118**, 3447-3507.
9. L. Zhu, M. Zhang, J. Xu, C. Li, J. Yan, G. Zhou, W. Zhong, T. Hao, J. Song, X. Xue, Z. Zhou, R. Zeng, H. Zhu, C.-C. Chen, R. C. I. MacKenzie, Y. Zou, J. Nelson, Y. Zhang, Y. Sun and F. Liu, *Nat. Mater.*, 2022, **21**, 656-663.
10. T. Chen, S. Li, Y. Li, Z. Chen, H. Wu, Y. Lin, Y. Gao, M. Wang, G. Ding, J. Min, Z. Ma, H. Zhu, L. Zuo and H. Chen, *Adv Mater*, 2023, **35**, 2300400.
11. K. Liu, Y. Jiang, F. Liu, G. Ran, F. Huang, W. Wang, W. Zhang, C. Zhang, J. Hou and X. Zhu, *Adv. Mater.*, 2023, **35**, 2300363.
12. S. Luo, C. Li, J. Zhang, X. Zou, H. Zhao, K. Ding, H. Huang, J. Song, J. Yi, H. Yu, K. S. Wong, G. Zhang, H. Ade, W. Ma, H. Hu, Y. Sun and H. Yan, *Nat. Commun.*, 2023, **14**, 6964.
13. H. Liang, X. Bi, H. Chen, T. He, Y. Lin, Y. Zhang, K. Ma, W. Feng, Z. Ma, G. Long, C. Li, B. Kan, H. Zhang, O. A. Rakitin, X. Wan, Z. Yao and Y. Chen, *Nat. Commun.*, 2023, **14**, 4707.
14. Y. Huang, E. J. Kramer, A. J. Heeger and G. C. Bazan, *Chem. Rev.*, 2014, **114**, 7006-7043.
15. L. Ye, H. Hu, M. Ghasemi, T. Wang, B. A. Collins, J. H. Kim, K. Jiang, J. H. Carpenter, H. Li, Z. Li, T. McAfee, J. Zhao, X. Chen, J. L. Y. Lai, T. Ma, J. L. Bredas, H. Yan and H. Ade, *Nat. Mater.*, 2018, **17**, 253-260.
16. M. Zhou, C. Liao, Y. Duan, X. Xu, L. Yu, R. Li and Q. Peng, *Adv. Mater.*, 2022, **35**, 2208279.
17. Y. Cai, Q. Li, G. Lu, H. S. Ryu, Y. Li, H. Jin, Z. Chen, Z. Tang, G. Lu, X. Hao, H. Y. Woo, C. Zhang and Y. Sun, *Nat. Commun.*, 2022, **13**, 2369.
18. X. Liu, C. Zhang, C. Duan, M. Li, Z. Hu, J. Wang, F. Liu, N. Li, C. J. Brabec, R. A. J. Janssen, G. C. Bazan, F. Huang and Y. Cao, *J. Am. Chem. Soc.*, 2018, **140**, 8934-8943.
19. K. Jiang, J. Zhang, C. Zhong, F. R. Lin, F. Qi, Q. Li, Z. Peng, W. Kaminsky, S.-H. Jang, J. Yu, X. Deng, H. Hu, D. Shen, F. Gao, H. Ade, M. Xiao, C. Zhang and A. K. Y. Jen, *Nat. Energy*, 2022, **7**, 1076–1086.
20. J. Zhang, S. Luo, H. Zhao, X. Xu, X. Zou, A. Shang, J. Liang, F. Bai, Y. Chen, K. S. Wong, Z. Ma, W. Ma, H. Hu, Y. Chen and H. Yan, *Angew. Chem. Int. Ed.*, 2022, **61**, e202206930.
21. A. Shang, S. Luo, J. Zhang, H. Zhao, X. Xia, M. Pan, C. Li, Y. Chen, J. Yi, X. Lu, W. Ma, H. Yan and H. Hu, *Sci. China Chem.*, 2022, **65**, 1758-1766.
22. W. Liang, L. Chen, Z. Wang, Z. Peng, L. Zhu, C. H. Kwok, H. Yu, W. Xiong, T. Li, Z. Zhang, Y. Wang, Y. Liao, G. Zhang, H. Hu and Y. Chen, *Adv. Energy Mater.*, 2024, **14**, 2303661.
23. T. Yang, C. Liao, Y. Duan, X. Xu, M. Deng, L. Yu, R. Li and Q. Peng, *Adv. Funct. Mater.*, 2022, **32**, 2208950.

24. L. Zhu, M. Zhang, W. Zhong, S. Leng, G. Zhou, Y. Zou, X. Su, H. Ding, P. Gu, F. Liu and Y. Zhang, *Energy Environ. Sci.*, 2021, **14**, 4341-4357.
25. K. An, W. Zhong, F. Peng, W. Deng, Y. Shang, H. Quan, H. Qiu, C. Wang, F. Liu, H. Wu, N. Li, F. Huang and L. Ying, *Nat. Commun.*, 2023, **14**, 2688.
26. Q. Zhang, M. A. Kelly, N. Bauer and W. You, *Acc. Chem. Res.*, 2017, **50**, 2401-2409.
27. S. C. Price, A. C. Stuart, L. Yang, H. Zhou and W. You, *J. Am. Chem. Soc.*, 2011, **133**, 4625-4631.
28. H. Lai, Q. Zhao, Z. Chen, H. Chen, P. Chao, Y. Zhu, Y. Lang, N. Zhen, D. Mo, Y. Zhang and F. He, *Joule*, 2020, **4**, 688-700.
29. T. Zhang, H. Chen, C. Li, K. Lu, L. Zhang, A. Shokrieh, J. Zhang, G. Lu, S. Lei and Z. Wei, *J. Mater. Chem. A*, 2022, **10**, 8837-8845.
30. Y. Cho, Z. Sun, K. M. Lee, G. Zeng, S. Jeong, S. Yang, J. E. Lee, B. Lee, S.-H. Kang, Y. Li, Y. Li, S. K. Kwak and C. Yang, *ACS Energy Lett.*, 2022, **8**, 96-106.
31. H. Chen, H. Lai, Z. Chen, Y. Zhu, H. Wang, L. Han, Y. Zhang and F. He, *Angew. Chem. Int. Ed.*, 2021, **60**, 3238-3246.
32. Y. Liu, D. Tang, K. Zhang, P. Huang, Z. Wang, K. Zhu, Z. Li, L. Yuan, J. Fan, Y. Zhou and B. Song, *ACS Omega*, 2017, **2**, 2489-2498.
33. J. Yuan, Y. Zhang, L. Zhou, G. Zhang, H.-L. Yip, T.-K. Lau, X. Lu, C. Zhu, H. Peng, P. A. Johnson, M. Leclerc, Y. Cao, J. Ulanski, Y. Li and Y. Zou, *Joule*, 2019, **3**, 1140-1151.
34. B. Carsten, J. M. Szarko, H. J. Son, W. Wang, L. Lu, F. He, B. S. Rolczynski, S. J. Lou, L. X. Chen and L. Yu, *J. Am. Chem. Soc.*, 2011, **133**, 20468-20475.
35. Y. Cui, H. Yao, J. Zhang, T. Zhang, Y. Wang, L. Hong, K. Xian, B. Xu, S. Zhang, J. Peng, Z. Wei, F. Gao and J. Hou, *Nat. Commun.*, 2019, **10**, 2515.
36. H. Hu, K. Jiang, P. C. Y. Chow, L. Ye, G. Zhang, Z. Li, J. H. Carpenter, H. Ade and H. Yan, *Adv. Energy Mater.*, 2018, **8**, 1701674.
37. Y. Lin, Y. Firdaus, F. H. Isikgor, M. I. Nugraha, E. Yengel, G. T. Harrison, R. Hallani, A. El-Labban, H. Faber, C. Ma, X. Zheng, A. Subbiah, C. T. Howells, O. M. Bakr, I. McCulloch, S. D. Wolf, L. Tsetseris and T. D. Anthopoulos, *ACS Energy Lett.*, 2020, **5**, 2935-2944.
38. L. Lu, T. Xu, W. Chen, E. S. Landry and L. Yu, *Nat. Photonics*, 2014, **8**, 716-722.
39. Z. Li, J. D. A. Lin, H. Phan, A. Sharenko, C. M. Proctor, P. Zalar, Z. Chen, A. Facchetti and T.-Q. Nguyen, *Adv. Funct. Mater.*, 2014, **24**, 6989-6998.
40. S. Chen, L. Hong, M. Dong, W. Deng, L. Shao, Y. Bai, K. Zhang, C. Liu, H. Wu and F. Huang, *Angew. Chem. Int. Ed.*, 2023, **62**, e202213869.
41. K. Yu, T. Zhou, W. Liang, X. Zhou, X. Xu, L. Yu, B. Hou, Y. Huang, F. Chen, Y. Liao and H. Hu, *ACS Appl. Mater. Interfaces*, 2023, **15**, 45158–45166.
42. F. Zhao, D. He, C. Zou, Y. Li, K. Wang, J. Zhang, S. Yang, Y. Tu, C. Wang and Y. Lin, *Adv. Mater.*, 2023, **35**, 2210463.
43. Y. Shao, Z. Xiao, C. Bi, Y. Yuan and J. Huang, *Nat. Commun.*, 2014, **5**, 5784.
44. J. Zhou, D. He, Y. Li, F. Huang, J. Zhang, C. Zhang, Y. Yuan, Y. Lin, C. Wang and F. Zhao, *Adv. Mater.*, 2023, **35**, 2207336.

45. C. M. Proctor, S. Albrecht, M. Kuik, D. Neher and T.-Q. Nguyen, *Adv. Energy Mater.*, 2014, **4**, 1400230.
46. V. V. Brus, C. M. Proctor, N. A. Ran and T.-Q. Nguyen, *Adv. Energy Mater.*, 2016, **6**, 1502250.
47. Y. Zeng, D. Li, Z. Xiao, H. Wu, Z. Chen, T. Hao, S. Xiong, Z. Ma, H. Zhu, L. Ding and Q. Bao, *Adv. Energy Mater.*, 2021, **11**, 2101338.
48. X. Zhang, C. Li, J. Xu, R. Wang, J. Song, H. Zhang, Y. Li, Y.-N. Jing, S. Li, G. Wu, J. Zhou, X. Li, Y. Zhang, X. Li, J. Zhang, C. Zhang, H. Zhou, Y. Sun and Y. Zhang, *Joule*, 2022, **6**, 444-457.
49. R. Wang, C. Zhang, Q. Li, Z. Zhang, X. Wang and M. Xiao, *J. Am. Chem. Soc.*, 2020, **142**, 12751-12759.
50. L. Zhan, S. Li, Y. Li, R. Sun, J. Min, Y. Chen, J. Fang, C. Q. Ma, G. Zhou, H. Zhu, L. Zuo, H. Qiu, S. Yin and H. Chen, *Adv. Energy Mater.*, 2022, **22**, 2201076.
51. H. Yu, Y. Wang, X. Zou, H. Han, H. K. Kim, Z. Yao, Z. Wang, Y. Li, H. M. Ng, W. Zhou, J. Zhang, S. Chen, X. Lu, K. S. Wong, Z. Zhu, H. Yan and H. Hu, *Adv. Funct. Mater.*, 2023, **33**, 2300712.
52. T. A. Dela Peña, J. I. Khan, N. Chaturvedi, R. Ma, Z. Xing, J. Gorenflot, A. Sharma, F. L. Ng, D. Baran, H. Yan, F. Laquai and K. S. Wong, *ACS Energy Lett.*, 2021, **6**, 3408-3416.
53. G. G. Malliaras, J. R. Salem, P. J. Brock and C. Scott, *Phys. Rev. B*, 1998, **58**, R13411-R13414.
54. D. Li, N. Deng, Y. Fu, C. Guo, B. Zhou, L. Wang, J. Zhou, D. Liu, W. Li, K. Wang, Y. Sun and T. Wang, *Adv Mater*, 2022, **35**, 2208211.
55. L. Ma, Y. Cui, J. Zhang, K. Xian, Z. Chen, K. Zhou, T. Zhang, W. Wang, H. Yao, S. Zhang, X. Hao, L. Ye and J. Hou, *Adv. Mater.*, 2022, **35**, 2208926.
56. T. Xiao, J. Wang, S. Yang, Y. Zhu, D. Li, Z. Wang, S. Feng, L. Bu, X. Zhan and G. Lu, *J. Mater. Chem. A*, 2020, **8**, 401-411.
57. S. Wu, *J. polym. sci., C Polym. symp.*, 1971, **34**, 19-30.
58. L. Ye, W. Zhao, S. Li, S. Mukherjee, J. H. Carpenter, O. Awartani, X. Jiao, J. Hou and H. Ade, *Adv. Energy Mater.*, 2016, DOI: 10.1002/aenm.201602000, 1602000.
59. Z. Wang, W. Liang, X. Zhou, S. Zhu, W. Xiong, J. Xu and H. Hu, *ACS Appl. Polym. Mater.*, 2023, **5**, 9329-9336.
60. H. Q. Liu, M. Y. Li, H. B. Wu, J. Wang, Z. F. Ma and Z. Tang, *J. Mater. Chem. A*, 2021, **9**, 19770-19777.
61. W. Shockley and H. J. Queisser, *J. Appl. Phys.*, 1961, **32**, 510-519.
62. N. A. Ran, S. Roland, J. A. Love, V. Savikhin, C. J. Takacs, Y. T. Fu, H. Li, V. Coropceanu, X. Liu, J. L. Bredas, G. C. Bazan, M. F. Toney, D. Neher and T. Q. Nguyen, *Nat. Commun.*, 2017, **8**, 79.
63. Y. Wang, J. Yu, R. Zhang, J. Yuan, S. Hultmark, C. E. Johnson, N. P. Gallop, B. Siegmund, D. Qian, H. Zhang, Y. Zou, M. Kemerink, A. A. Bakulin, C. Müller, K. Vandewal, X.-K. Chen and F. Gao, *Nat. Energy*, 2023, **8**, 978–988.

- The data supporting this article have been included as part of the Supplementary Information.